Appl Phys B (2009) 96: 325–335
DOI 10.1007/s00340-009-3505-0

Applied Physics B
Lasers and Optics

Near-field optical power transmission of dipole nano-antennas

K. Şendur · E. Baran

Received: 4 December 2008 / Revised version: 1 March 2009 / Published online: 3 April 2009

Abstract Nano-antennas in functional plasmonic applications require high near-field optical power transmission. In this study, a model is developed to compute the near-field optical power transmission in the vicinity of a nano-antenna. To increase the near-field optical power transmission from a nano-antenna, a tightly focused beam of light is utilized to illuminate a metallic nano-antenna. The modeling and simulation of these structures is performed using 3-D finite element method based full-wave solutions of Maxwell's equations. Using the optical power transmission model, the interaction of a focused beam of light with plasmonic nano-antennas is investigated. In addition, the tightly focused beam of light is passed through a band-pass filter to identify the effect of various regions of the angular spectrum to the near-field radiation of a dipole nano-antenna. An extensive parametric study is performed to quantify the effects of various parameters on the transmission efficiency of dipole nano-antennas, including length, thickness, width, and the composition of the antenna, as well as the wavelength and half-beam angle of incident light. An optimal dipole nano-antenna geometry is identified based on the parameter studies in this work. In addition, the results of this study show the interaction of the optimized dipole nano-antenna with a magnetic recording medium when it is illuminated with a focused beam of light.

PACS 73.20.Mf · 85.70.Sq · 68.37.Uv · 84.40.Ba · 42.79.Vb

K. Şendur (✉) · E. Baran
Faculty of Engineering and Natural Sciences, Sabanci University, Orhanli-Tuzla, 34956 Istanbul, Turkey
e-mail: sendur@sabanciuniv.edu

1 Introduction

Existing and emerging nano-optical applications, such as scanning near-field optical microscopy [1], data storage [2], nano-lithography [3], and bio-chemical sensing [4] have two main requirements: an optical spot beyond the diffraction limit and a high transmission efficiency. Nano-antennas [5–7] can be used in nano-optical systems due to their ability to obtain very small optical spots. Optical antennas have a long history and there are many experimental works in the literature including early optical rectification works [8–10] and more recent resonant antennas [11–14]. The ability of nano-antennas to obtain optical spots beyond the diffraction limit is not sufficient for their utilization in practical plasmonic applications. In addition to a very small optical spot, a nano-antenna should provide high transmission efficiency for practical applications. The transmission efficiency of a nano-antenna determines the data transfer rate of storage devices and the scan times of near-field optical microscopes. Therefore, the transmission efficiency of nano-antennas should be quantified and optimized for potential utilization in practical applications. A thorough assessment of the near-field transmission efficiency of nano-antennas is crucial for understanding their potential and limitations for emerging plasmonic applications.

Metallic nano-antennas hold the promise of providing high transmission efficiency [5] that can enable emerging plasmonic applications. Therefore, the extension of the detailed understanding of antennas at the macroscale to that of the nanoscale is of great interest. The interaction of antennas with electromagnetic waves has been thoroughly investigated at microwave frequencies. Simple scaling rules that were obtained at microwave frequencies, however, do not hold at optical frequencies [15]. There are two main differences between the underlying physics of the interaction

of light with metallic nano-antennas at microwave and optical frequencies: (1) contrary to their behavior at microwave frequencies, at optical frequencies metallic antennas support surface plasmons [15–18], and (2) the skin-depth of metals at optical frequencies is significantly larger than those at microwave frequencies in terms of electrical dimensions.

Previous works in the literature have considered power transmission efficiency and focused beams [2, 19–22]. In previous works, the focused beams were treated as linearly polarized plane waves and Gaussian beam profiles [2, 19–21]. Plane waves and Gaussian beams become less accurate approximations for a focused beam of light as the beam becomes more tightly focused. The angular spectrum of a plane wave is composed of a single point in k-space. In other words, the angular spectrum of a plane wave is infinitesimally narrow. A tightly focused beam of light, on the other hand, has a wide angular spectrum. As a result, a plane wave approximation becomes less accurate as the beam becomes more tightly focused. A Gaussian beam approximation is valid in the paraxial limit. As the beam becomes more tightly focused, the paraxial approximation is no longer valid. At this point, the Gaussian beam approximation also becomes an inadequate model of a highly focused beam [23]. Richards-Wolf theory [24, 25] provides an accurate representation of an incident beam near the focus of an aplanatic lens. Therefore, it is desirable to quantify the associated near-field optical power transmission of dipole nano-antennas, particularly when the structures are illuminated with a tightly focused beam of light as described by Richards–Wolf theory. It is also desirable to identify the effects of various regions of the angular spectrum on the near-field radiation of a dipole nano-antenna. This can be achieved by applying a band-pass filter to the tightly focused beam of light to suppress undesired components.

In this study, a detailed derivation of the near-field optical power transmission in the vicinity of a nano-antenna is given. The findings of this study allow the assessment of the suitability of nano-antennas for potential use in practical plasmonic applications. Using the power transmission calculations, a comprehensive and detailed analysis of the parameters affecting the near-field radiation of a nano-antenna is provided. An optimal dipole nano-antenna geometry is identified based on the parameter studies conducted in this study. In addition, the tightly focused beam of light is passed through a band-pass filter to identify the effect of various regions of the angular spectrum to the near-field radiation of a dipole nano-antenna. In Sect. 2 we present the mathematical formulations for the near-field optical power transmission of nano-antennas when they are illuminated with a focused beam of light. The incident electric field is obtained from the numerical aperture of the lens system and operating wavelength. The scattered and total components of the electric fields are obtained using the interaction of the incident field and the nano-antenna. The field quantities are transformed into power quantities using the method described in Sect. 2 along with 3-D finite element method based[1] [26] full-wave solutions of Maxwell's equation. In Sect. 3, an extensive parametric study is performed to quantify the effects of material and geometrical parameters on the near-field power transmission of dipole nano-antennas. The optimum geometry and the corresponding power transmission are studied for various parameters including length, thickness, width, and composition of the antenna, as well as the wavelength of incident light. The near-field distributions are presented for the optimized structures in Sect. 3. Concluding remarks appear in Sect. 4.

2 Near-field optical power transmission

An important criterion when assessing the performance of a nano-optical antenna for potential utilization in a functional plasmonic application is the near-field optical power transmission. In a functional plasmonic application, the transmission efficiency can be defined as the ratio of power transmitted to the sample over the optical power input to the system. A nano-antenna with low transmission efficiency may prevent its use in a practical applications since it determines key metrics in a system, such as the data transfer rate of storage devices and the scan times of near-field optical microscopes. One method of increasing the power transmission is to increase the input power, however, it is limited by the power of the laser diodes that are available. In addition, high input power usually results in power dissipation in the metallic parts, which can cause significant heating and structural deformation of the nano-optical transducers [27]. Therefore, a nano-antenna with high transmission efficiency is more feasible to increase the transmitted output power in practical applications.

One possible method of further improving the transmitted power to the sample is to utilize a tightly focused beam of incident light onto the antenna. As the incident electromagnetic radiation becomes more tightly focused, the spot size of the diffraction limited radiation incident onto the nano-antenna reduces. Reducing the spot size of the incident radiation increases the magnitude of the incident electric field illuminating the nano-antenna. Since the incident electric field illuminating the nano-antenna increases, the near-field radiation from the nano-antenna also increases. Therefore, a tightly focused beam of incident light exciting the antenna can be used to further improve the near-field optical power transmission.

[1] All the FEM calculations in this report are performed with High Frequency Structure Simulator (HFSS^{TM}) from Ansoft Inc. with the in-house developed focused beam models integrated into it.

Near-field optical power transmission is not only a function of antenna parameters such as geometry and material properties, but is also related to the focused beam parameters such as the numerical aperture of the beam and operating wavelength. Although there has been much effort to understand the effect of various parameters related to near-field radiation from nano-antennas, the studies in the literature do not include detailed descriptions of a focused beam of light. In the literature a plane wave is usually used to represent the incident beam of light to understand the interaction of incident beam and nano-antennas. If the incident optical beam becomes more tightly focused, a plane wave representation becomes inaccurate for modeling a focused beam of light. Therefore, near-field transmitted optical power calculations involving focused light are of great interest to assess the performance of nano-antennas in functional plasmonic applications.

In this section, we first present a brief summary of the incident focused beam model based on the Richards–Wolf theory [24, 25]. After that, we present a model to compute the near-field transmitted power starting from the incident optical beam definition and nano-antenna parameters.

The Richards–Wolf theory [24, 25] provides an accurate representation of an incident beam near the focus of an aplanatic lens. Using the Richards–Wolf vector field representation [24, 25], the total electric field in the vicinity of the focus is given by

$$\mathbf{E}(\mathbf{r}_p) = -\frac{i}{\lambda}\int_0^{\alpha} d\theta \sin\theta \int_0^{2\pi} d\phi\, \mathbf{a}(\theta,\phi)\exp(-i\mathbf{k}\cdot\mathbf{r}_p), \tag{1}$$

where α is the half angle of the beam, $\mathbf{r}_p$ is the observation point

$$\mathbf{r}_p = x_p\hat{x} + y_p\hat{y} + z_p\hat{z} = r_p\cos\phi_p\hat{x} + r_p\sin\phi_p\hat{y} + z_p\hat{z} \tag{2}$$

and

$$\mathbf{k} = \frac{2\pi}{\lambda}(\sin\theta\cos\phi\hat{x} + \sin\theta\sin\phi\hat{y} - \cos\theta\hat{z}). \tag{3}$$

In (2) and (3) λ is the wavelength in the medium, $r_p = \sqrt{x_p^2 + y_p^2}$, and $\phi_p = \arctan(y_p/x_p)$. In (1), $\mathbf{a}(\theta,\phi)$ is the weighting vector, which is given as

$$\mathbf{a}(\theta,\phi) = \begin{bmatrix} \cos\theta\cos^2\phi + \sin^2\phi \\ \cos\theta\cos\phi\sin\phi - \cos\phi\sin\phi \\ \sin\theta\cos\phi \end{bmatrix}\sqrt{\cos\theta}. \tag{4}$$

To obtain the electric field distributions, (1) can be evaluated using a numerical integration [28]. Sample electric field distributions can be found in the literature [23, 28, 29].

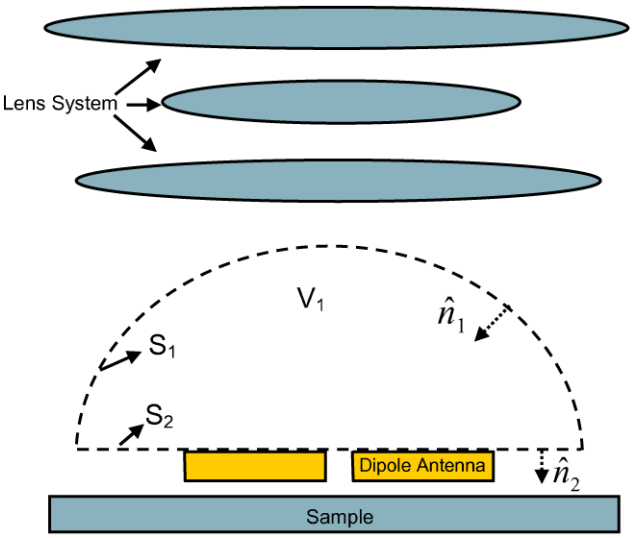

Fig. 1 A schematic illustration of a dipole antenna and sample object illuminated with a focused beam of incident light from a lens system. The sample object is in the near-field of the nano-antenna. V_1 is an semi-spherical volume that will be utilized in the power calculations

A typical nano-antenna configuration with respect to the lens system and sample is illustrated in Fig. 1. The nano-antenna is in the near-field of the sample object. The nano-antenna is illuminated with a focused beam of light that is obtained using a lens system. In this figure, V_1 is a semi-spherical volume that will be utilized in the power calculations. V_1 can either be a vacuum or a high-index transparent material. If a far field excitation is utilized, then V_1 is represented as a vacuum. To further increase the incident electric field, a solid immersion lens can be utilized on top of a nano-antenna. In this case V_1 is composed of a high-index transparent dielectric. In this figure S_1 represents the curved hemispherical surface, and S_2 represents the planar surface that forms the bottom surface of volume V_1. As shown in Fig. 1, $\hat{n}_1$ and $\hat{n}_2$ represent the normal directions to the surfaces S_1 and S_2, respectively.

The total electric field $\mathbf{E}^t(\mathbf{r})$ is composed of two components,

$$\mathbf{E}^t(\mathbf{r}) = \mathbf{E}^i(\mathbf{r}) + \mathbf{E}^s(\mathbf{r}), \tag{5}$$

where $\mathbf{E}^i(\mathbf{r})$ and $\mathbf{E}^s(\mathbf{r})$ are the incident and scattered electric field components, respectively. The incident electric field can be defined as the electric field propagating in space in the absence of the scattering object. In this problem, the incident field is the optical beam generated by the lens system in the absence of the nano-antenna and sample in Fig. 1. In other words, the incident field can be considered as the focused beam propagating in free space as show in Fig. 2. The scattered electric field $\mathbf{E}^s(\mathbf{r})$ in (5) represents the fields resulting from the interaction of the incident field $\mathbf{E}^i(\mathbf{r})$ with the scattering objects, which in our case, are composed of

the nano-antenna and sample. As shown in (5), the total field is the summation of the incident and scattered field components.

For the power conversion, scaling factors will be based on the incident fields. These scaling factors will later be utilized to adjust the electric field magnitudes of scattered and total electric field quantities. The incident field geometry is shown in Fig. 2. By utilizing Poynting's theorem [30, 31] for the incident field geometry we obtain

$$P_z = \mathrm{Re}\left[\int\int_{S_1}\left(\frac{1}{2}\mathbf{E^i}(\mathbf{r})\times\mathbf{H^{i*}}(\mathbf{r})\right)\cdot\hat{n}_1\,dS\right] - \int\int\int_{V_1}\sigma\left|\mathbf{E^i}(\mathbf{r})\right|^2 dV. \tag{6}$$

In (6), P_z is the power propagating in the $\hat{z}$-direction. In this equation, $E_x^i(\mathbf{r})$ is the electric field defined by (1) for vacuum and the second term is zero since $\sigma = 0$ in vacuum. In the case where V_1 represents a solid immersion lens, the electric field representation by Ichimura et al. [32] should be utilized instead of (1).

To obtain the scattered field, $\mathbf{E}^s(\mathbf{r})$, we used a 3-D finite element method (FEM) based full-wave solution of Maxwell's equations [26]. To represent the scattering geometries accurately, tetrahedral elements are used to discretize the computational domain. Radiation boundary conditions are used in FEM simulations. On the tetrahedral elements, edge basis functions, and second-order interpolation functions are used to expand the functions. Adaptive mesh refinement is used to improve the coarse solution regions with high field intensities.

Once the scattered field is solved via FEM, the total field can be obtained using (5). Finally, to convert the $\mathbf{E}^t(\mathbf{r})$ to the correct power quantities, the fields should be multiplied by

$$\sqrt{\frac{\text{Actual Input Optical Power}}{P_z}}. \tag{7}$$

This power conversion will be utilized in the results to adjust the power quantities to express the actual input power entered into the system. Once this power conversion is performed, the total power dissipation in the sample can be obtained by

$$\text{Dissipated Power in the Sample} = \int\int\int_{V_s}\sigma\left|E^t(\mathbf{r})\right|^2 dV, \tag{8}$$

where V_s represents the hot spot in the sample volume. Assuming V_1 in (6) is vacuum, then the transmission efficiency is given as

$$\text{Transmission Efficiency} = \frac{\int\int\int_{V_s}\sigma|E^t(\mathbf{r})|^2\,dV}{\int\int_{S_1}(\frac{1}{2}\mathbf{E^i}(\mathbf{r})\times\mathbf{H^{i*}}(\mathbf{r}))\cdot\hat{n}_1\,dS}. \tag{9}$$

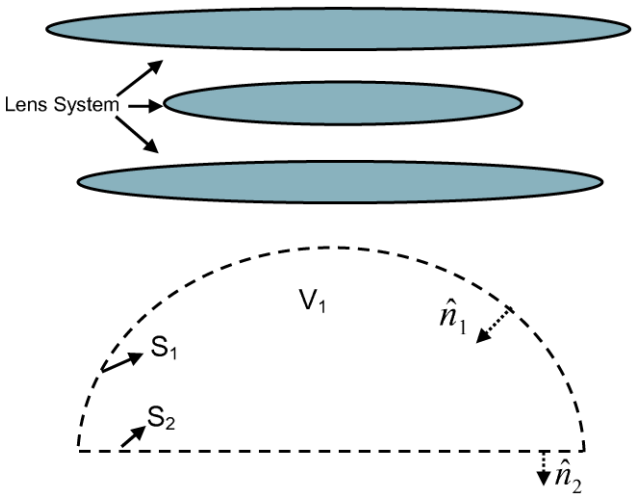

Fig. 2 A schematic illustration of the incident field $\mathbf{E}^i(\mathbf{r})$ in the absence of any scattering objects

3 Dipole nano-antennas

To couple incident electromagnetic energy with small scale electronic devices, antennas have been utilized. The antennas achieve this coupling by localizing the incident radiation to dimensions smaller than the wavelength. The coupling mechanism between small scale electronic devices and antennas at radio and microwave frequencies has been well understood. A similar coupling mechanism is applicable between nano-antennas operating at optical frequencies and objects with feature dimensions below the diffraction limit. At optical frequencies, nanoscale metallic antennas can be utilized to couple incident optical beams to length scales much smaller than the diffraction limit.

A metallic dipole nano-antenna, shown in Fig. 3, primarily utilizes evanescent waves to couple electromagnetic energy to a sample in the near-field. The direction of the polarization of the incident radiation and the antenna geometry play an important role in this process. If the incident polarization is along the long-axis of the antenna as shown in

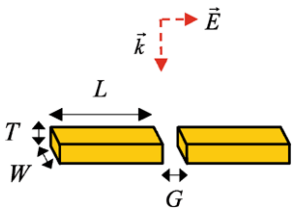

Fig. 3 A schematic illustration of a dipole antenna and its dimensions. The antenna is illuminated with incident electromagnetic radiation shown as $\mathbf{E}(\mathbf{r})$

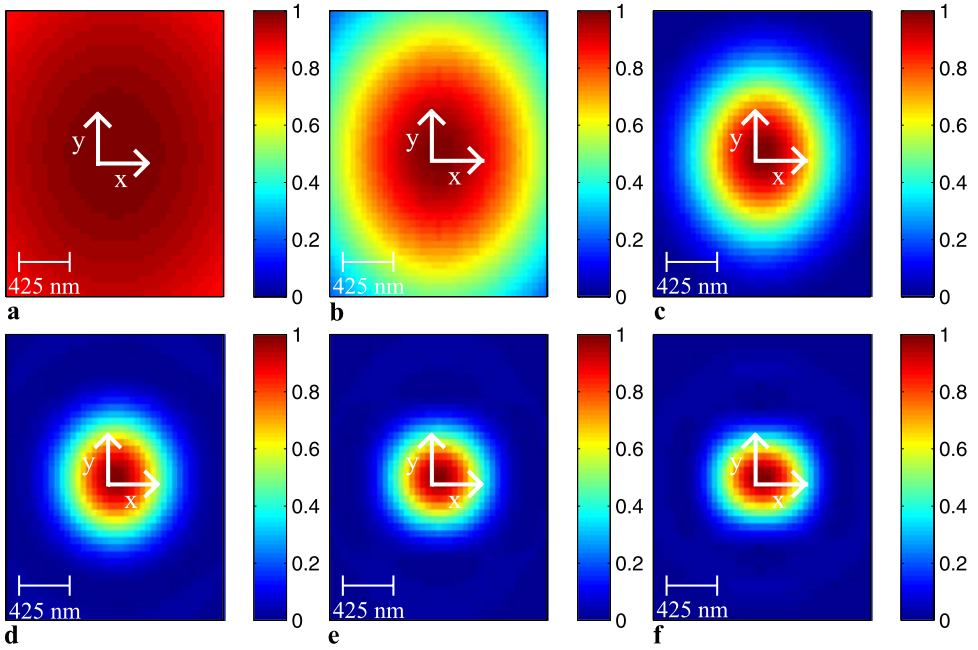

Fig. 4 Incident $|E|^2$ distribution in the absence of antennas. The fields are plotted at the focal plane $\hat{x}$–$\hat{y}$ for various half-beam angles α of the incident beam: (**a**) $\alpha = 5°$, (**b**) $\alpha = 15°$, (**c**) $\alpha = 30°$, (**d**) $\alpha = 45°$, (**e**) $\alpha = 60°$, and (**f**) $\alpha = 75°$

Fig. 3, then the incident electromagnetic radiation creates induced currents along this axis in the antenna. These induced currents are the source of charge accumulation at the ends of the antenna. The charges created across the gap separating the metallic parts of the antenna have opposite polarity. The oscillation of the charges with opposite polarity is the source of localized near-field electromagnetic radiation. This localized near-field radiation is composed of propagating and evanescent components. If a structure is brought into the near-field of this gap, then the electromagnetic fields radiating due to this charge oscillation interact with the structure. The evanescent component of the electromagnetic field is particularly important in achieving high power transmission from the antenna.

The interaction between the antenna and the sample structure at visible and optical frequencies leads to interesting applications, including near-field optical microscopy [1] and data storage [2]. At visible and infrared frequencies, however, the underlying physics of the interaction of light with metallic nano-antennas is complicated due to surface plasmon effects [15–18]. In addition, at these frequencies the incident electromagnetic field interacts with the entire antenna structure due to the large skin-depth of metals at optical frequencies (in terms of electrical dimensions). As a result of the geometry-dependent plasmonic effects, the antenna shape and composition play an important role. If the shape and composition of the metallic structures and the wavelength of the incident radiation are appropriately chosen, then it is possible to excite plasmon resonances over the metallic particles that form the nano-antenna. Size- and shape-dependent surface plasmon resonances of nanoparticles [33, 34] can be excited if the frequency of the incident radiation matches the frequency of the oscillation of the free-electron gas of the metal forming the nano-antenna. Surface plasmon resonances are associated with large electric field enhancement, which is of particular interest for applications that require high transmission efficiency.

Figure 4 illustrates the focused incident $|E^i|^2$ distributions onto the dipole nano-antennas. The fields are plotted at the focal plane $\hat{x}$–$\hat{y}$ for various half-beam angles. For small α, the field distribution is similar to that of a plane wave. As α increases, the beam becomes more tightly focused. In Fig. 5, the total $|E^t|^2$ distribution for a dipole antenna is shown on the $\hat{x}$–$\hat{z}$ cut plane when it is illuminated with the focused beams shown in Fig. 4. For this particular simulation, the sizes of the antenna are $L = 110$, $T = 20$, $W = 20$, and $G = 20$ nm. In this simulation, the incident focused beam is polarized in the $\hat{x}$-direction, and propagates in the negative $\hat{z}$-direction. The wavelength of the incident light is 850 nm. The antenna is placed at the focus of the incident beam, which is also the global origin for the simulations. The optical properties of metals used in this study are retrieved from the literature [35]. The peak value of the graphs in Fig. 5 represents the intensity enhancement, which is defined as

$$\text{Intensity enhancement} = \frac{|E^t(0,0,0)|^2}{|E^i(0,0,0)|^2}. \tag{10}$$

In other words, total intensity $|E^t|^2$ at the antenna gap center is normalized to the value of the incident intensity $|E^i|^2$ at the focus. The results in Fig. 5 show a confined electric field close to the gap region of the antenna. A large electric field enhancement is also observed for all the half-beam angle values α. The intensity enhancement at the center of the

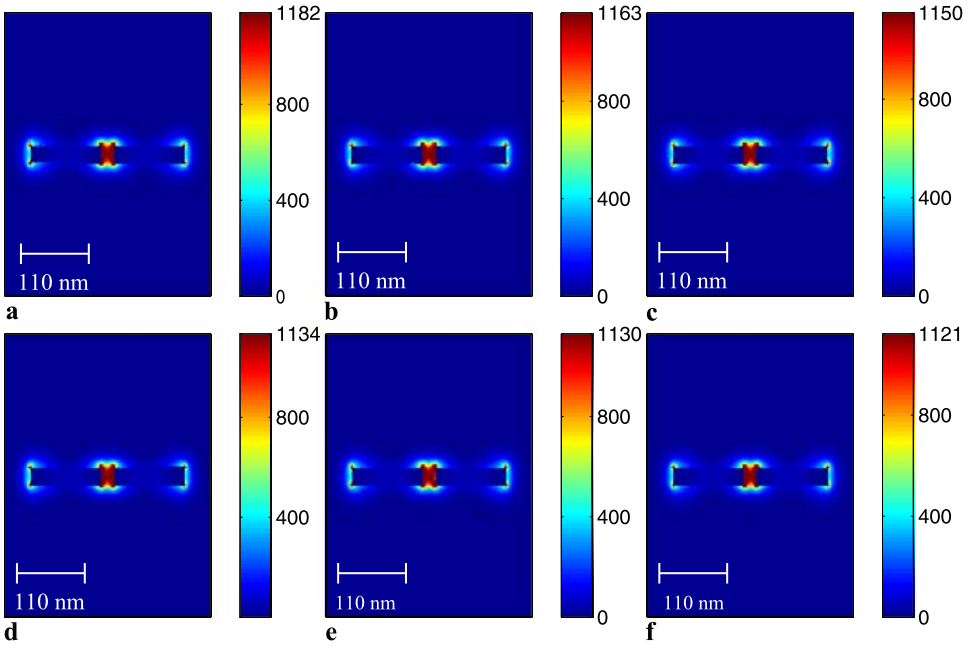

Fig. 5 Total $|E|^2$ distribution in the presence of nano-antennas. The fields are plotted on the $\hat{x}$–$\hat{z}$ cut plane for various half-beam angle α of the incident beam: (**a**) $\alpha = 5°$, (**b**) $\alpha = 15°$, (**c**) $\alpha = 30°$, (**d**) $\alpha = 45°$, (**e**) $\alpha = 60°$, and (**f**) $\alpha = 75°$

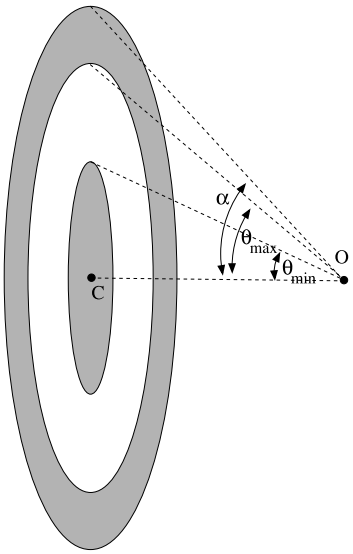

Fig. 6 A band-pass filter suppresses the $\theta < \theta_{\min}$ and $\theta > \theta_{\max}$ part of the angular spectrum. The *dark regions* indicate the parts of the angular spectrum that are suppressed. Point O represents the focal point of the lens and point C represents the center of the lens

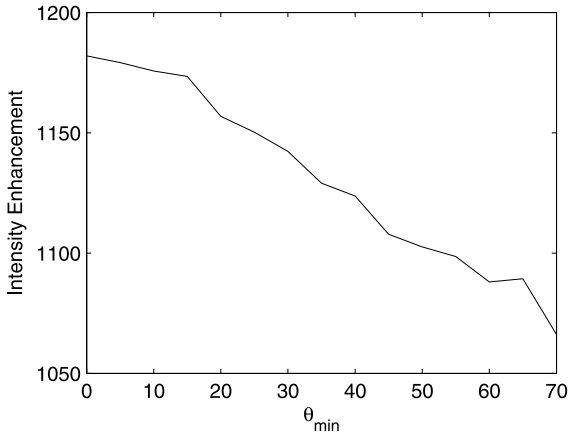

Fig. 7 Intensity enhancement as a function of $\theta_{\min}$. In this calculation the cut-off angle is selected as $\theta_{\max} = \theta_{\min} + 5°$

antenna is about 1200 for small α. The intensity enhancement slowly reduces to 1100 as α is increased.

The results in Fig. 5 indicate that the contribution from the rays with large incident angles is less than the contribution from the rays with small incident angles. To provide further evidence for this observation, the incident beam is separated into angular spectral bands. The contribution due to each spectral band is then calculated separately. To achieve this, the incident beam is passed through an angular band-pass filter as shown in Fig. 6. The filter suppresses the $\theta < \theta_{\min}$ and $\theta > \theta_{\max}$ part of the angular spectrum. In this calculation, spectral bands with 5° intervals are considered, which corresponds to $\theta_{\max} = \theta_{\min} + 5°$. Intensity enhancement is plotted as a function of $\theta_{\min}$ in Fig. 7. The results suggest that the intensity enhancement due to rays with large incident angles is less than the intensity enhancement from the rays with small incident angles.

As mentioned above, the results in Fig. 5 indicate that the intensity enhancement is almost preserved as α increases. The output power, however, not only depends on the intensity enhancement but also on the intensity of the incident focused beam. As shown in Fig. 8, the intensity of the incident focused beam $|E^i(0,0,0)|^2$ increases with increasing α. The incident beam becomes more tightly focused with

increasing α, which increases the incident electric field intensity, as shown in Fig. 8. As a result, the output intensity increases as α increases. This suggests that significant gains can be achieved by increasing the α despite a small reduction in the transmission efficiency.

We next plot the electric field at the center of the antenna as a function of the incident wavelength and antenna length. To achieve this, we performed simulations by varying the incident wavelength from 400 to 2000 nm by intervals of 50 nm. At each wavelength, we performed simulations by changing the antenna length. The intensity at the center of the gap, $|\mathbf{E}(x = 0, y = 0, z = 0)|^2$, is calculated for each wavelength and antenna length. By recording the intensity over the rectangular grid shown in Fig. 9, we formed the surface graphs. In this simulation, an incident optical beam with a power of 100 mW is used. The numerical aperture of the lens system is assumed as 0.86. In Fig. 9 it should be noted that the $|\mathbf{E}(x = 0, y = 0, z = 0)|^2$ values do not correspond to the intensity enhancement. The large $|\mathbf{E}(x = 0, y = 0, z = 0)|^2$ values are a results of both intensity enhancement and large incident field value corresponding to 100 mW incident power and 0.86 numerical aperture. In Fig. 9, the intensity, $|\mathbf{E}(x = 0, y = 0, z = 0)|^2$, is plotted as a function of wavelength and antenna length for a gold antenna with other parameters set as $T = 10$, $W = 10$, and $G = 20$ nm. Figure 10 shows the results for $T = 20$, $W = 20$, and $G = 20$ nm and Fig. 11 for the parameters $T = 50$, $W = 50$, and $G = 20$ nm.

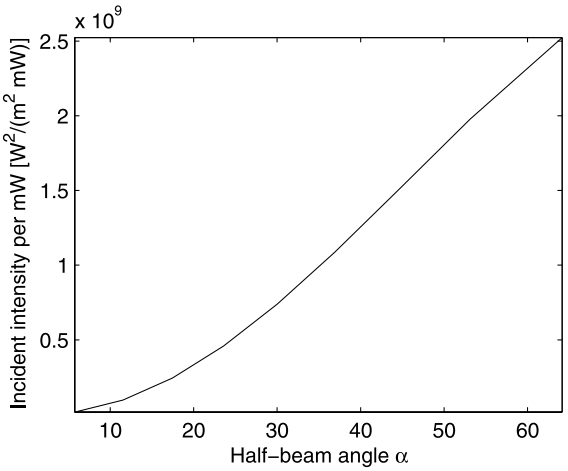

Fig. 8 Incident intensity per mW incident power as a function of half-beam angle for $\lambda = 850$ nm

The important information found on the surface plots is the optimum length of the antenna and the corresponding intensity values at various wavelengths. Figures 12(a) and (b) illustrate the optimum length and corresponding intensity values extracted from surface plots for gold dipole antennas with various cross sections. In Fig. 12(a), the optimum length of the antenna is plotted as a function of wavelength, and in Fig. 12(b) the corresponding intensity values are plotted as a function of wavelength. The simulations are repeated for a dipole antenna made of silver with the same dimensions. The optimum length and the corresponding intensity values for a silver dipole antenna are plotted as a function of wavelength in Figs. 13(a) and (b), respectively.

The results in Figs. 12 and 13 point to some important conclusions regarding optimum antenna length and thickness as a function of wavelength. L_{opt} versus wavelength graphs in Figs. 12(a) and 13(a) suggest that the optimum antennas are longer for thicker antennas. This result can best be interpreted with the effect of the geometric aspect ratio of nanoparticles on plasmon resonances. As discussed by Kelly et al. [33], the plasmon resonances of nanoparticles shift toward longer wavelengths as the aspect ratio of the particle is increased. Such a trend agrees with the findings observed in dipole nano-antennas, which are composed of two nanoparticles. A thin nano-antenna is composed of nanoparticles

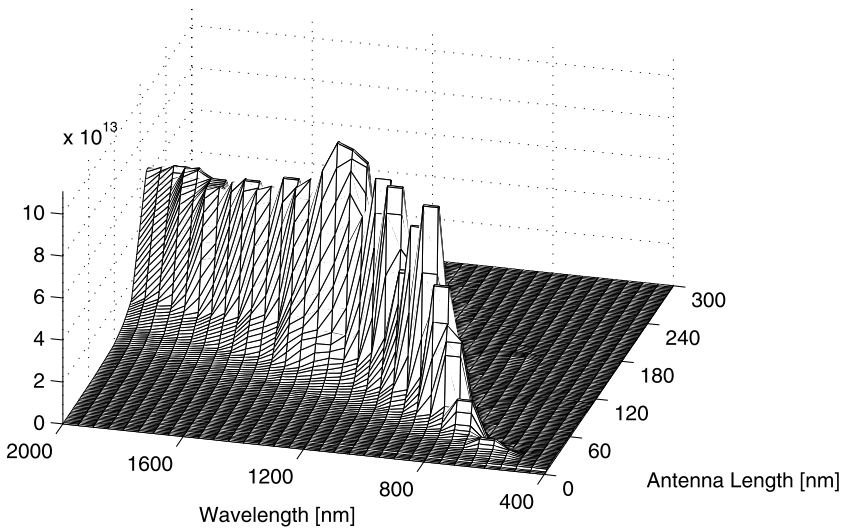

Fig. 9 The intensity at the gap center, $|\mathbf{E}(x = 0, y = 0, z = 0)|^2$, for a gold dipole antenna as a function of wavelength and antenna length. The dimensions of the gold dipole antenna are selected as: $T = 10$, $W = 10$, and $G = 20$ nm

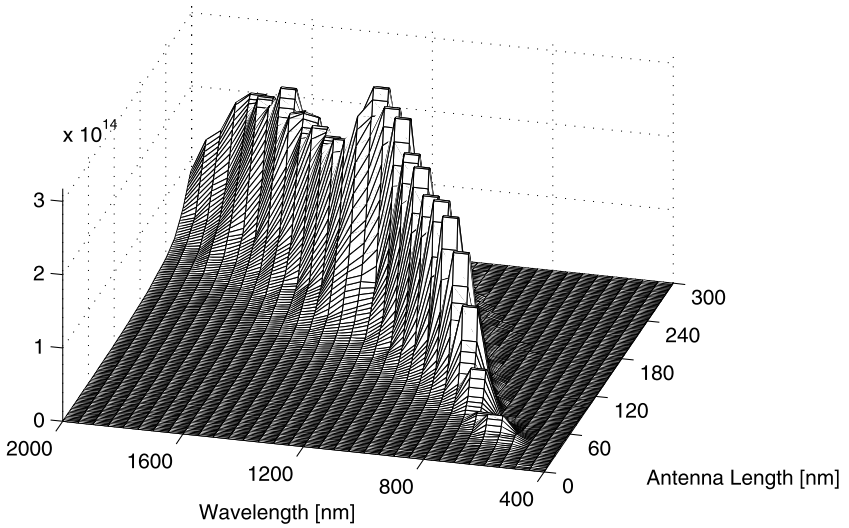

Fig. 10 The intensity at the gap center, $|\mathbf{E}(x = 0,\ y = 0,\ z = 0)|^2$, for a gold dipole antenna as a function of wavelength and antenna length. The dimensions of the gold dipole antenna are selected as: $T = 20$, $W = 20$, and $G = 20$ nm

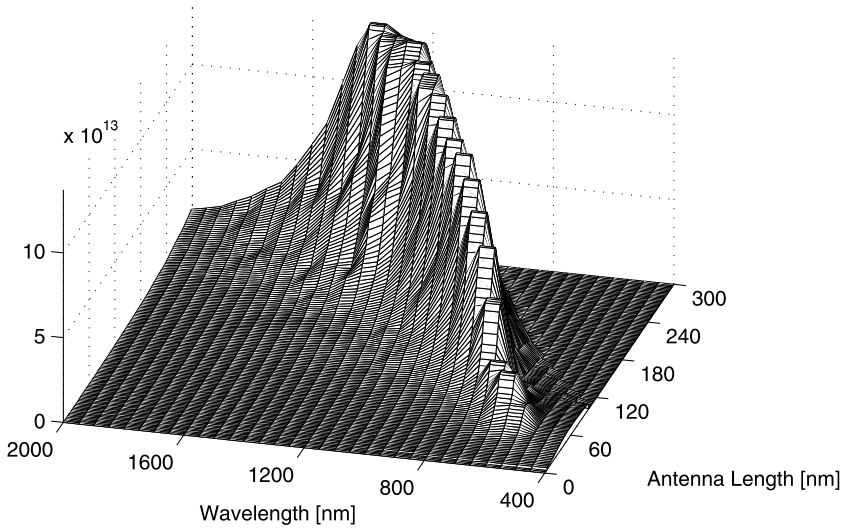

Fig. 11 The intensity at the gap center, $|\mathbf{E}(x = 0,\ y = 0,\ z = 0)|^2$, for a gold dipole antenna as a function of wavelength and antenna length. The dimensions of the gold dipole antenna are selected as: $T = 50$, $W = 50$, and $G = 20$ nm

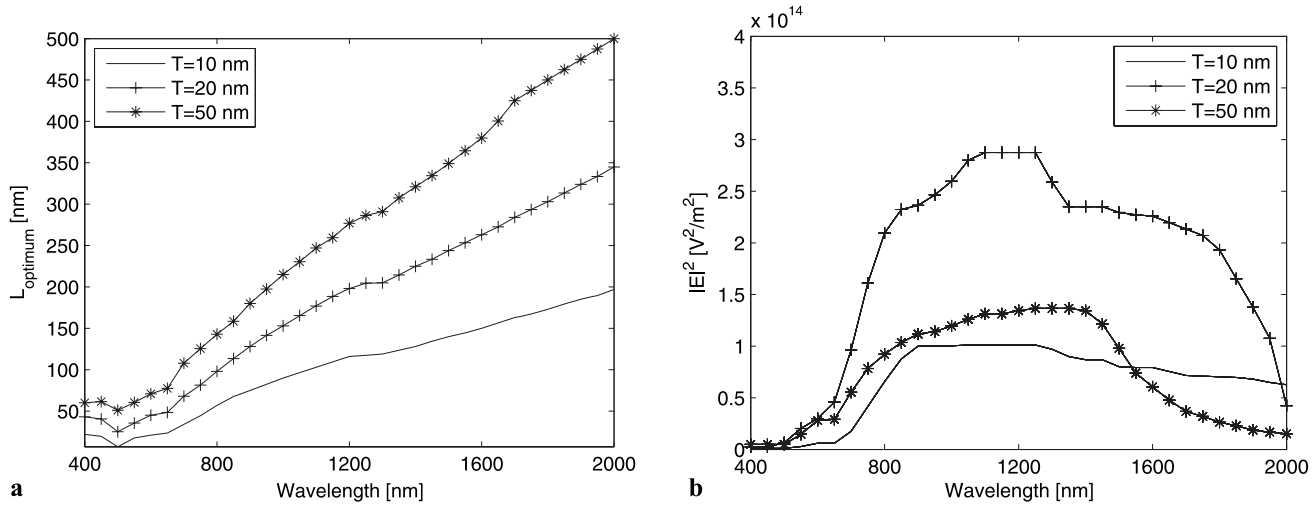

Fig. 12 (**a**) Optimum gold dipole antenna lengths as a function of frequency are plotted for various antenna thicknesses. (**b**) Optimum intensity values $|\mathbf{E}(x = 0,\ y = 0,\ z = 0)|^2$ for optimum antenna lengths are plotted as a function of wavelength for various antenna thicknesses

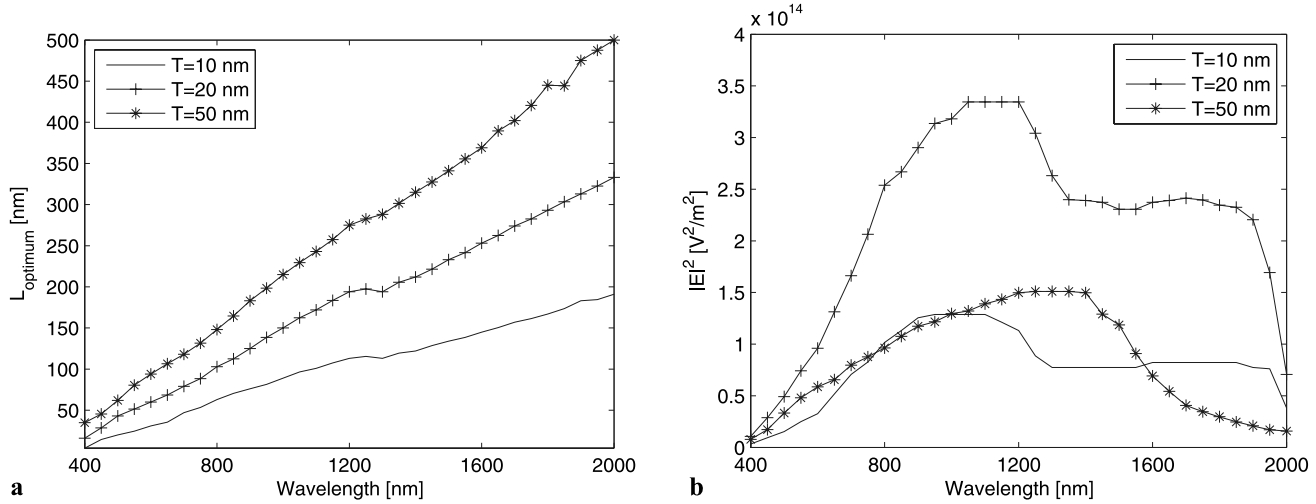

Fig. 13 (**a**) Optimum silver dipole antenna lengths as a function of frequency are plotted for various antenna thicknesses. (**b**) Optimum intensity values $|\mathbf{E}(x=0, y=0, z=0)|^2$ for optimum antenna lengths are plotted as a function of wavelength for various antenna thicknesses

with a larger aspect ratio than a thick nano-antenna. This results in a shift of resonances toward longer wavelengths, which result in a less steep L_{opt} versus wavelength curve as shown in Figs. 12(a) and 13(a). The corresponding optimum $|\mathbf{E}(x=0, y=0, z=0)|^2$ values in Figs. 12(b) and 13(b) show that the optimum thickness for the nano-antennas is around 20 nm. The corresponding $|\mathbf{E}(x=0, y=0, z=0)|^2$ is higher for 20 nm compared with antenna thicknesses of 10 and 50 nm. This is due to the interaction of surface plasmons associated with the top and bottom surfaces of the nano-antennas. The surface plasmons can be excited on both surfaces of thin films, causing the surface plasmons on both surfaces to interact with each other [17]. This interaction results in an optimum antenna thickness around 20 nm to obtain the best power transmission as shown in Figs. 12(b) and 13(b).

The L_{opt} versus wavelength graphs in Figs. 12(a) and 13(a) show linear behavior, as initially predicted by Novotny [15]. In Fig. 12(a) the L_{opt} versus wavelength graph for gold shows deviations from the linear behavior around a wavelength of 500 nm due to intraband transitions of gold, which are at similar wavelengths predicted in the literature [15]. For silver, the transitions occur below 400 nm, therefore, it is not observed in Fig. 13(a). There is another deviation from linear behavior in Figs. 12(a) and 13(a) around 1200 nm. These deviations from linear behavior are not present in the literature [15]. We found that the main reason for this deviation from linear behavior around 1200 nm is due to the frequency-dependent experimental material properties that were used in our model. The refractive index of gold and silver are obtained from the experimental data from Palik [35], which shows a discontinuity around 1200 nm. This is the main reason for the deviation from the linear behavior in Figs. 12(a) and 13(a). This deviation is not predicted in the literature by a Drude model [15], which extrapolates the single frequency measurement to other frequencies.

The L_{opt} versus wavelength graphs in Figs. 12(a) and 13(a) show smaller L_{opt} values than those predicted in the literature [15]. There are two primary reasons for this difference. The results in the literature only consider plasmon propagation when predicting the optimum points, neglecting the poles generated at the ends of the antenna due to the finite size of the structures. These poles impact the plasmon resonance conditions. The presence of the poles at the end of the nano-antenna creates a depolarizing field due to the surface charges at the end of the antenna. Surface charges that accumulate at the interface between the nano-antenna and the surrounding vacuum result in a shape-dependent field. As a result, the charge distribution within the nano-antenna realigns so that it opposes the shape-dependent depolarizing field. This causes the frequency of the charge oscillation to increase, which results in the optimum antenna length becoming shorter since the optimum antenna length corresponds to half of the period of the charge oscillation. This is the main difference between the results in Figs. 12(a) and 13(a) as compared to the literature. Another factor that causes the difference is the finite size gap between the metallic structures. The effect of the gap can be neglected in antenna applications in microwave frequencies, since it is very small in electrical dimensions. However, for optical and infrared frequencies, the impact of the gap cannot be neglected since its electrical dimension is considerable. When the gap is extremely small, the metallic particles that form the antenna are strongly coupled. They act together resulting in a longer resonant structure. As the gap dimension gets electrically larger, which is the case at optical frequencies, the response of the particles starts to decouple. This results in

shorter resonant structures, and therefore, shorter optimum lengths observed in Figs. 12(a) and 13(a).

Thus far, the results for the L_{opt} values at various wavelengths have been presented. The results, however, do not provide sufficient information to decide which of these L_{opt} and wavelength pairs provide the best conditions for strong near-field radiation. To reach this conclusion, the $|\mathbf{E}(x=0, y=0, z=0)|^2$ corresponding L_{opt} were plotted in Figs. 12(b) and 13(b), which provide the near-field radiation from the antenna at various frequencies. This data is complementary to the L_{opt} data presented in Fig. 12(a) and 13(a). The L_{opt} at various wavelengths are obtained from Fig. 12(a) and 13(a), however, the information with regards to the best wavelength for near-field radiation is obtained from Figs. 12(b) and 13(b). The $|\mathbf{E}(x=0, y=0, z=0)|^2$ data complement our previous L_{opt} versus wavelength graphs and the literature [15].

Due to the different material properties of gold and silver, their viability for use in nano-antennas is affected. A comparison of the results for gold and silver nano-antennas in Figs. 12(a) and 13(a) suggests that the optimum length for silver nano-antennas suggest slightly shorter optimum lengths compared to that of gold nano-antennas. The reason for this minor difference between the optimum length of silver and gold nano-antennas is not clear. A comparison of the results Figs. 12(b) and 13(b) suggest that silver nano-antennas provide a slightly better optical power transmission compared to gold nano-antennas. Although silver has slightly better optical power transmission performance, it is also reactive and can tarnish on the scale of nanometers. Since the difference between the optical performance is not drastically different, gold seems to be a better choice for nano-antennas in practical plasmonic applications.

In the literature, the field enhancement is typically used to assess the performance of a nano-antenna. Although high field enhancement is desirable in various applications, information about the field enhancement is not sufficient to assess the capability of a nano-antenna in some applications. The optical power transmission from a nano-antenna to a sample is a more suitable assessment metric for nano-antennas, since it is used as the driving force in other physical processes.

Next, we calculate the optical power transmission to the sample by obtaining the dissipated power distribution in a sample object when it is placed in the vicinity of an optimal dipole nano-antenna with parameters selected according to the results of this study. The geometry of the problem is shown in Fig. 1. Based on the results of this study, we selected a gold dipole nano-antenna operating at a wavelength of 1100 nm with the following dimensions: $L = 175$, $T = 20$, $W = 20$, and $G = 20$ nm. For the sample structure we selected a 20 nm cobalt layer, which is a metal typically utilized in near-field data storage. The sample is located 10 nm away from the antenna. Figure 14 illustrates the

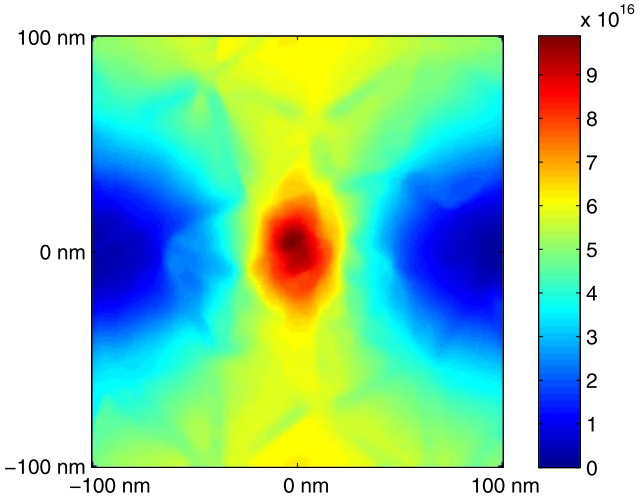

Fig. 14 Dissipated power per 1 mW incident power [W/(m^3 mW)] in the sample when the nano-antenna is 10 nm away from the sample

power distribution dissipated in the sample, i.e. $\sigma|\mathbf{E}(\mathbf{r})|^2$. The volume for the transmission efficiency calculation is selected as the 35 nm×35 nm×10 nm cobalt volume, which is immediately under the optical hot spot. By integrating the dissipated power distribution in that volume, we found that about 0.1% of the incident power is transferred to the sample. As a point of reference, the power transfer efficiency for the case of a focused beam without the antenna is calculated as 0.024% for the same 35 nm×35 nm×10 nm cobalt volume.

4 Conclusion

In this work, a formulation was provided to convert electric field quantities to optical power quantities for nano-antennas starting from Poynting's theorem. This formulation was used to quantify the near-field optical power transmission of optimum dipole antenna structures when the incident beam is a tightly focused beam of light. To find an optimal dipole nano-antenna, an extensive parametric study was performed to quantify the effects of material and geometrical parameters on transmission efficiency. The near-field optical power transmission was studied for various parameters including length, thickness, width, and composition of the antenna as well as the wavelength of incident light. Our results suggest that the optimum antenna lengths are smaller than suggested in the literature [15] due to the effects of interacting poles and the finite gap between metallic structures. Based on the parameters studied in this work, an optimal nano-antenna was identified. The dissipated power density distribution within the near-field sample was presented for an optimal dipole antenna.

Acknowledgements The authors would like to thank Güllü Kiziltaş for her support of this work and many helpful discussions. This work was performed with the support of the European Community Marie Curie International Reintegration Grant (IRG) Agreement Number MIRG-CT-2007-203690.

References

1. A. Hartschuh, E.J. Sánchez, X.S. Xie, L. Novotny, Phys. Rev. Lett. **90**, 095503 (2003)
2. K. Sendur, W. Challener, C. Peng, J. Appl. Phys. **96**, 2743–2752 (2004)
3. L. Wang, X. Xu, J. Microsc. **229**, 483–489 (2008)
4. B. Liedberg, C. Nylander, I. Lundstroem, Sens. Actuators **4**, 299–304 (1983)
5. R.D. Grober, R.J. Schoelkopf, D.E. Prober, Appl. Phys. Lett. **70**, 1354–1356 (1997)
6. K. Sendur, W. Challener, J. Microsc. **210**, 279–283 (2003)
7. E.X. Jin, X. Xu, J. Comput. Theor. Nanosci. **5**, 214–218 (2008)
8. S. Wang, Appl. Phys. Lett. **28**, 303 (1976)
9. V. Daneu, D. Sokoloff, A. Sanchez, A. Javan, Appl. Phys. Lett. **15**, 398 (1969)
10. A. Sanchez, C.F. Davis Jr., K.C. Liu, A. Javan, J. Appl. Phys. **49**, 5270 (1978)
11. K.B. Crozier, A. Sundaramurthy, G.S. Kino, C.F. Quate, J. Appl. Phys. **94**, 4632 (2003)
12. D.P. Fromm, A. Sundaramurthy, P.J. Schuck, G. Kino, W.E. Moerner, Nano Lett. **4**, 957 (2004)
13. P. Muhlschlegel, H.-J. Eisler, O.J.F. Martin, B. Hecht, D.W. Pohl, Science **308**, 1607–1609 (2005)
14. F. Jackel, A.A. Kinkhabwala, W.E. Moerner, Chem. Phys. Lett. **446**, 339–343 (2007)
15. L. Novotny, Phys. Rev. Lett. **98**, 266802 (2007)
16. H. Raether, *Surface Plasmons on Smooth and Rough Surfaces and on Gratings* (Springer, Berlin, 1988)
17. J.J. Burke, G.I. Stegeman, T. Tamir, Phys. Rev. B **33**, 5186–5201 (1986)
18. H. Raether, *Physics of Thin Films* (Academic Press, New York, 1977), pp. 145–261
19. T. Matsumoto, T. Shimano, H. Saga, H. Sukeda, J. Appl. Phys. **95**, 3901–3906 (2004)
20. T. Matsumoto, Y. Anzai, T. Shintani, K. Nakamura, T. Nishida, Opt. Lett. **31**, 259–261 (2006)
21. A. Itagi, D. Stancil, J. Bain, T. Schlesinger, Appl. Phys. Lett. **83**, 4474 (2003)
22. K. Sendur, C. Peng, W. Challener, Phys. Rev. Lett. **94**, 043901 (2005)
23. L. Novotny, B. Hecht, *Principles of Nano-Optics* (Cambridge University Press, New York, 2006), Chap. 3
24. E. Wolf, Proc. R. Soc. Lond. Ser. A **253**, 349–357 (1959)
25. B. Richards, E. Wolf, Proc. R. Soc. Lond. Ser. A **253**, 358–379 (1959)
26. J.M. Jin, *The Finite Element Method in Electromagnetics* (Wiley, New York, 2000)
27. R.M. Stöckle, N. Schaller, V. Deckert, C. Fokas, R. Zenobi, Opt. Lett. **20**, 970 (1995)
28. K. Sendur, W. Challener, O. Mryasov, Opt. Express **16**, 2874–2886 (2008)
29. K.S. Youngworth, T.G. Brown, Opt. Express **7**, 77–87 (2000)
30. D.K. Cheng, *Field and Wave Electromagnetics* (Addison-Wesley, New York, 1983)
31. C.A. Balanis, *Advanced Engineering Electromagnetics* (Wiley, New York, 1989)
32. I. Ichimura, S. Hayashi, G.S. Kino, Appl. Opt. **36**, 4339–4348 (1997)
33. K.L. Kelly, E. Coronado, L.L. Zhao, G.C. Schatz, J. Phys. Chem. B **107**, 668–677 (2003)
34. J.P. Kottmann, O.J.F. Martin, Appl. Phys. B **73**, 299–304 (2001)
35. E.D. Palik, *Handbook of Optical Constants of Solids* (Academic Press, San Diego, 1998)